

www.advenergymat.de

Surface Design with Cation and Anion Dual Gradient Stabilizes High-Voltage LiCoO₂

Weiyuan Huang, Qi Zhao, Mingjian Zhang,* Shenyang Xu, Haoyu Xue, Chen Zhu, Jianjun Fang, Wenguang Zhao, Guoxi Ren, Runzhi Qin, Qinghe Zhao, Haibiao Chen, and Feng Pan*

LiCoO₂ (LCO) is the most successful cathode material for commercial lithium-ion batteries. Cycling LCO to high potentials up to 4.5 V or even 4.6 V can significantly elevate the capacity but cause structural degradation due to the serious surface side reaction between the highly oxidized Co4+ and O-species with organic electrolytes. To tackle this concern, a new strategy, constructing cation and anion dual gradients at the surface of LCO (DG-LCO), is proposed. Specifically, the electrochemically inactive cation and anion are selected to substitute Co3+ and O2- at the surface in a gradated manner, thus minimizing the highly oxidized Co4+ and O-species at high potentials and suppressing the induced surface side reactions. Unexpectedly, this dual gradient design leads to a spinel-like surface structure coherently with bulk layered structure, which facilitates Li+ diffusion kinetics. Thus, DG-LCO achieves high capacity and excellent cycling stability at 4.6 V (≈216 mA h g⁻¹ at 0.1 C, a capacity retention of 88.6% after 100 cycles in 1.8 A h pouch full cell at 1 C), as well as improved rate capability (≈140 mA h g⁻¹ at 5 C). These studies provide useful guidelines for future design of cathode materials with long lifespan and high rate capability.

1. Introduction

Driven by the pressing demands for high energy density in portable electronics, the cathode materials in lithium-ion batteries are desired to have a large capacity and a high operating voltage. [1] Considering the high tap density of the micrometer-size single crystals,^[2] LiCoO₂ (LCO) is advantageous in terms of volumetric

W. Huang, Q. Zhao, M. Zhang, S. Xu, H. Xue, C. Zhu, J. Fang, W. Zhao, R. Qin, Q. Zhao, F. Pan

School of Advanced Materials

Peking University Shenzhen Graduate School

Shenzhen 518055, China

E-mail: zhangmj@pkusz.edu.cn; panfeng@pkusz.edu.cn

State Key Laboratory of Functional Materials for Informatics Shanghai Institute of Microsystem and Information Technology Chinese Academy of Sciences

Shanghai 200050, China

H. Chen

Institute of Marine Biomedicine Shenzhen Polytechnic

Shenzhen 518055, China

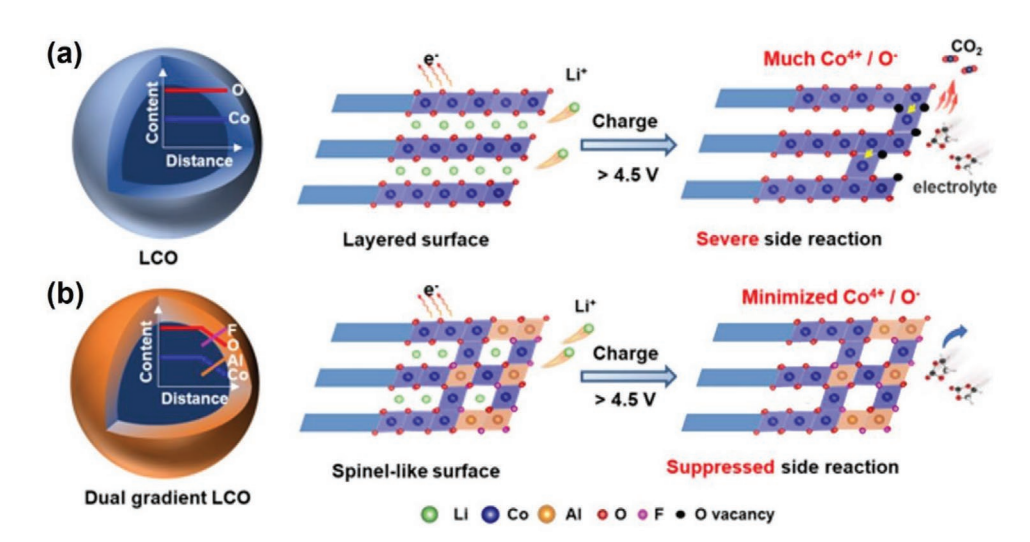
The ORCID identification number(s) for the author(s) of this article can be found under https://doi.org/10.1002/aenm.202200813.

DOI: 10.1002/aenm.202200813

energy density among the reported cathode materials, thus dominates the current battery market for electronics.[3,4] The practical reversible capacity of LCO is only ≈160 mA h g⁻¹ with a cutoff voltage of 4.35 V, far below the theoretical capacity (274 mA h g⁻¹), thus there is still a large space for expanding the capacity.^[5,6] Further increasing the charging cutoff voltage is the most effective approach to extract more Li⁺ from the LCO framework.^[7,8] For example, La- and Al-co-doped LCO offered an initial capacity of ≈190 mA h g⁻¹ with a cut-off voltage of 4.5 V and retained 96% capacity after 50 cycles,[9] and Ti-Mg-Al co-doped LCO offered an initial capacity of 202 mA h g-1 with a cut-off voltage of 4.6 V and retained 86% capacity after 100 cycles.[10] However, the origin of structural stability by these trace doping remains unclear, which restricts the further development of high-voltage LCO.

Our recent work revealed the structural differences between regular LCO and high-voltage LCO at the atomic level, and correlated the curvature of the Co-O layers near the surface with structural instability.[11] Li's group reported a hybrid Co cation and O anion redox occurred at a high voltage of 4.6 V.[12] As shown in Scheme 1a, the generated Co4+ and O species at high potentials would induce the severe surface side reactions, including the catalytic decomposition of the carbonate-based electrolyte, and the lattice O loss in the form of CO2. Such O loss would lead to the irreversible Co migration, formation of dense Co₃O₄ spinel phase at the surface that would block Li+ diffusion,[13] and lattice distortion in the bulk evolving into microcracks upon cycling.[14] Aiming to effectively resolve these critical issues, surface engineering is proved to be a direct and efficient strategy.^[15] Lu's group reported the ternary lithium, aluminum, fluorine-modified LCO with improved cycling stability when operating at 4.6 V.[16] However, the active material was covered with a large amount of Al₂O₃ and LiAlO₂ particles rather than a uniform coating layer, and it was still susceptible to HF attack from the electrolyte, thus the interfacial stability and structural integrity deteriorated upon longterm cycling. LCO with modified surface by electrochemically stable solid electrolyte Li_{1.4}Al_{0.4}Ti_{1.6}(PO₄)₃ was prepared through mechanical mixing followed by a high-temperature annealing process to mitigate the catalytic effect of surficial Co⁴⁺ species at

16146840, 2022, 20, Downloaded from https://advanced.on.inlibitary.viley.com/ob/10.1002/aem....20220813 by University Town Of Shezzhen, Wiley Online Library on [23/1/12025]. See the Terms and Conditions (https://onlinelibrary.wiley.com/rems-and-conditions) on Wiley Online Library for rules of use; OA articles are governed by the applicable Centwive Commons I



Scheme 1. Surface design of cation and anion dual gradient for LCO. a) Regular LCO, showing severe surface side reactions due to the highly oxidized Co⁴⁺ and O⁻ species at high potentials. b) Cation and anion dual gradient LCO with the minimized Co⁴⁺ and O⁻ species, showing suppressed side reactions at high potentials.

high voltages. [17] Coating with metal oxides, [18] fluorides, [19] and phosphates [20] was also investigated for surface passivation, but the coating layer cannot fully cover the surface of LCO particles due to the structural incoherency. [4,21] Li's group prepared LCO single crystals with a semi-coherent LiMn_{1.5}Ni_{0.5}O₄ spinellike shell by means of an electrochemical method to extend the operating voltage to 4.6 V. [22] However, it is difficult to control the electrochemical-induced surface spinel phase to achieve a homogenous surface phase transformation.

Aiming to solve the concerns induced by the surficial Co⁴⁺ and O- species (Scheme 1a), we proposed a directed cation and anion dual gradient strategy for the surface modification of LCO (DG-LCO). As Al3+ and Co3+ have similar ionic radii (0.535 and 0.545 Å, respectively) and the same valence, it allows for a wide scope of Al substitution into LCO lattice. The large Al-O bonding energy and smaller change in crystal dimension made Al³⁺ substituted LCO exhibit the improved structure stability and the lower lattice strain upon charge and discharge process.^[23] F surface doping can mitigate the interfacial side reaction with the electrolyte, as F participates into forming a more stable transition metal (TM)-F bond that can directly modify the anionic oxidation process at high charge voltage. [24] Furthermore, it could generate surficial TMF_x species as one of the favorable components of cathode-electrolyte interphase (CEI), which can effectively resist the corrosion of HF in electrolyte, thus protect the cathode surface from HF attack and improve the CEI stability. [25] Accordingly, as shown in Scheme 1b, the electrochemically inactive cation and anion, Al3+ and F- here, were selected to gradiently substitute Co3+ and O2- at the surface, thus minimizing the highly oxidized Co⁴⁺ and O⁻ species at near-surface region when charged to high potentials, and greatly suppressing the induced surface side reactions, which is the key to maintain the structure stability of LCO at high potentials. Furthermore, the gradient surface exhibited a co-lattice spinel future, which facilitated interfacial Li+ transfer and mitigated the structure collapse in deep charge state. All these factors synergistically contribute to the substantially improved

cyclic stability and rate capability of DG-LCO at high operating voltages. This strategy opens new opportunities to develop high-performance cathode materials for commercial lithiumion batteries.

2. Results and Discussion

2.1. Dual Gradient Co-Lattice Spinel Surface

DG-LCO was prepared through a simple wet-coating process followed by medium-temperature calcination for bare LCO. The crystal structures of bare LCO and DG-LCO were investigated by X-ray diffraction (XRD) measurement. As shown in Figure 1, all Bragg diffraction peaks can be well indexed to the typical layered α -NaFeO₂ structure with a space group of R-3m without detectable impurities. [26] The obvious decrease in the ratio of (003)/(104) peak intensities may be ascribed to the much more random stacking among DG-LCO single crystals. The Rietveld refinement results (Figure S1 and Table S1, Supporting Information) present nearly the same lattice parameters for bare LCO and DG-LCO, hinting little influence on bulk structure. Scanning electron microscopy (SEM) images indicate that, DG-LCO does not exhibit obvious morphology change as compared with bare LCO (Figure S2, Supporting Information). The elemental distribution was visualized by energy dispersive spectrometer (EDS) mapping (Figures S3 and S4, Supporting Information). Inductively coupled plasma optical emission spectroscopy (ICP-OES) results (Table S2, Supporting Information) and the EDS spectrum fitting results (Table S3, Supporting Information) indicate that, the total doping content of Al and F are very low. To determine the distribution of the doping elements inside the particle, a cross-section sample was prepared by the focused ion beam (FIB) for EDS mapping. It is clear that, Al and F elements are enriched at the near-surface region within a thickness of about 60 nm (Figure 1b,c), hinting a gradient elemental doping. The molar ratio of Co/Al/F is 1/0.22/0.23 (Table S4, Supporting

16146840, 2022, 20, Downloaded from https://adv:

on Wiley Online Library for rules of use; OA articles are governed by the applicable Creative Commons

www.advancedsciencenews.com

www.advenergymat.de

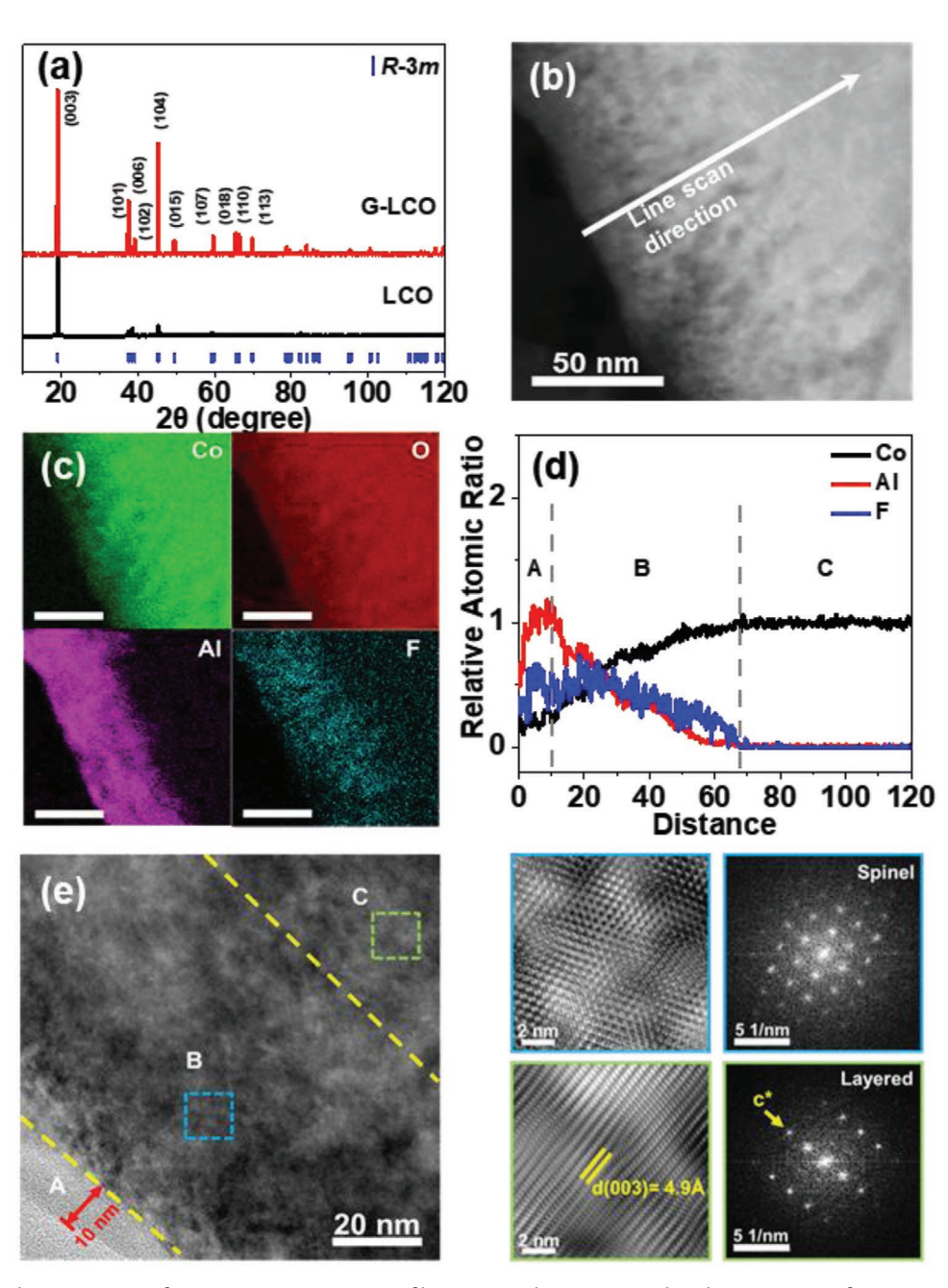


Figure 1. Structure characterization of DG-LCO. a) XRD patterns of bare LCO and DG-LCO powders. b) TEM image of DG-LCO cross-section sample by FIB and c) the corresponding EDS mapping images. d) The elemental distribution along the depth based on the EDS line scan data. e) HRTEM image of the DG-LCO cross-section sample. The selected regions were enlarged and transformed to FFT maps on the right panel.

Information), further confirming the local enrichment of Al and F. To quantitatively analyze the elemental distribution along the depth, EDS line scanning was carried out along the white arrow in Figure 1b. As shown in Figure 1d, according to the relative elemental content, the depth profile can be divided into three regions. Region A is an ≈ 10 nm outermost layer of Li-Al-O-F with a constant atomic ratio. Region B is an ≈ 60 nm layer with Li-Al-Co-O-F elemental gradient, wherein Al and F contents gradually decrease in contrast to the gradual increase of Co content, confirming the implementation of cation and anion dual gradient. In Region C, there was a constant content

of Co, reflecting the pure LCO bulk without Al and F elements. High-resolution transmission electron microscopy (HRTEM) images and the selected-region FFT maps in Figure 1e were used to analyze the local structures. Region I exhibits a low degree of crystallinity, hinting the amorphous character of the Li-Al-O-F layer. The selected region in the cyan rectangle was zoomed in and FFT transformed on the right panel. The images reveal the typical spinel structure. TEM electron energy loss spectra (EELS) show that (Figure S5, Supporting Information), Li signal persists from the surface to the bulk, along with O and Co signals. It confirms that, Li_xCoO₂-type spinel-like surface

16146840, 2022, 20, Downloaded from https://advancec

.com/doi/10.1002/aenm.202200813 by University Town Of Shenzhen, Wiley Online Library on [23/11/2025]. See the Terms

and-conditions) on Wiley Online Library for rules of use; OA articles are governed by the applicable Creative Commons

www.advancedsciencenews.com

www.advenergymat.de

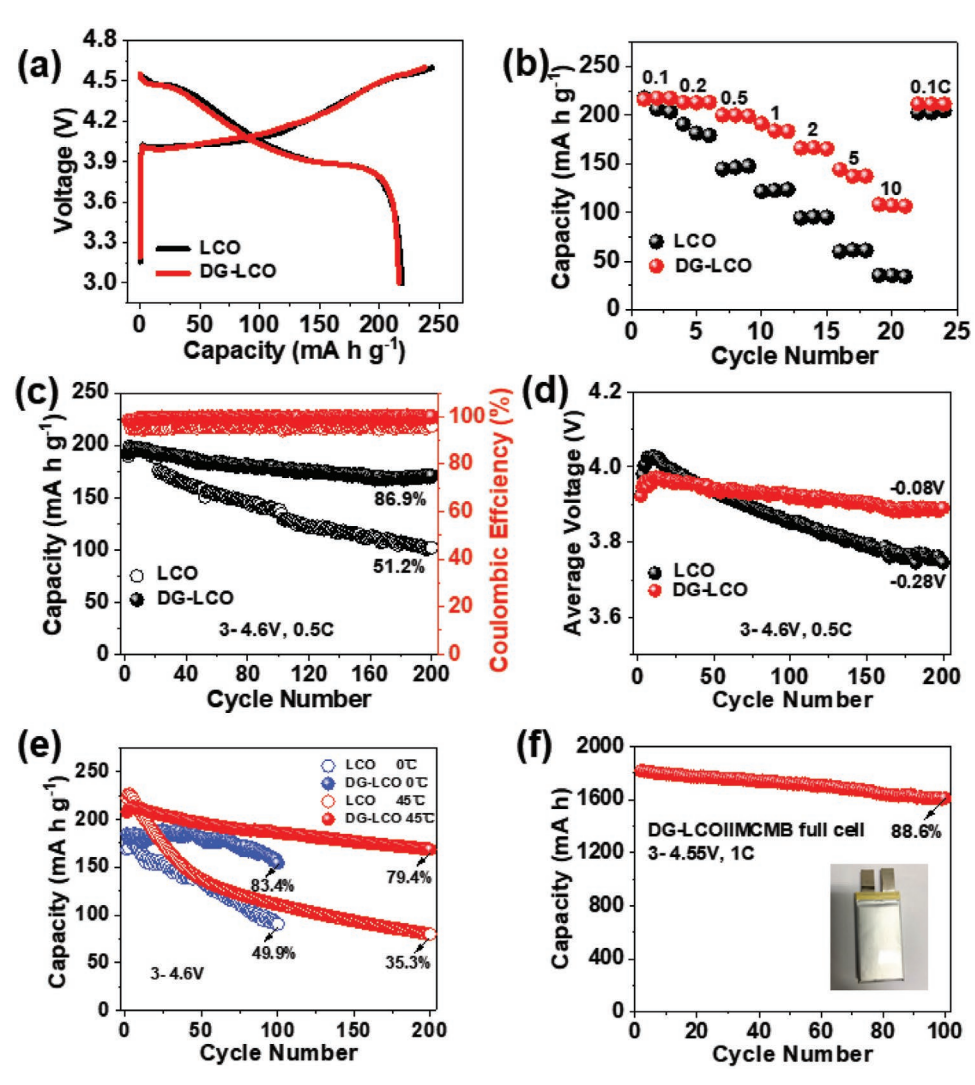


Figure 2. Improved electrochemical performance of DG-LCO. a) The first charge/discharge profiles of bare LCO and DG-LCO within 3.0–4.6 V at 0.1 C. b) Rate performance of bare LCO and DG-LCO cathodes. c) Cycling performance of bare LCO and DG-LCO at room temperature within 3.0–4.6 V at 0.5 C and d) corresponding average voltage change upon cycling. e) Cycling performance of bare LCO and DG-LCO at 0 °C (0.2 C) and 45 °C (2 C) within 3.0–4.6 V. f) Cycling performance of DG-LCO pouch full cell within 3.0–4.55 V (equivalent to 3.05–4.6 V vs Li/Li⁺) at 1 C.

structure formed in DG-LCO rather than dense Co_3O_4 , which can help to enhance the Li diffusion due to the intrinsic 3D Li⁺ diffusion channels in spinel phase. [27] Similar process was performed for the green rectangle in Region III, and a typical layered structure with a (003) spacing of 4.8 Å was identified, same with bare LCO (Figure S6, Supporting Information), further confirming the intact bulk structure. Above observations strongly confirmed that, dual gradient spinel-like surface with a thickness of \approx 60 nm was uniformly and coherently integrated on crystalline LCO.

2.2. Improved Electrochemical Performance

The electrochemical performance of bare LCO and DG-LCO was first evaluated in half cells between 3.0 and 4.6 V. The first charge–discharge profiles in **Figure 2**a show the high discharge capacity of 218 and 216 mA h g $^{-1}$ at 0.1 C (1 C = 200 mA g $^{-1}$)

for bare LCO and DG-LCO, respectively. The dQ/dV results in Figure S7 (Supporting Information) were deduced from the charge-discharge profiles. Three oxidation peaks at 3.8, 4.1, and 4.4 V can be related to the continuous phase transition from H2 to M1, M1 to H3, H3 to H1-3 (M2), respectively. [5,28] The similar phenomenon is observed in the cyclic voltammetry (CV) curves (Figure S8, Supporting Information). Upon the CV test process, the cathode suffers from shallow charge and discharge, namely, Li+ intercalation/deintercalation at the particle near-surface region, thus CV is sensitive to the electrochemical behavior in the near-surface region while the dQ/dV curve reflects the bulk behavior. Different from the dQ/dV curves, the reduction peaks in the CV curves for DG-LCO were sharper than those for LCO, indicating a faster Li⁺ diffusion kinetics in DG-LCO, especially at the surface. The Li+ diffusion coefficients in bare LCO and DG-LCO were determined by the galvanostatic intermittent titration technique (GITT). As shown in Figure S9b (Supporting Information), the Li+ diffusion coefficient for DG-LCO

16146480, 2022, 20, Downloaded from https://advanced onlinelibrary.wiely.com/doi/10.1002/aem.m.202200813 by University Town Of Shenzhen, Wiley Online Library on [23/11/2025]. See the Terms and Conditions (https://onlinelibrary.wiely.com/terms-and-conditions) on Wiley Online Library for rules of use; OA archies are governed by the applicable Centwive Commons I

was calculated to be $\approx 1.12 \times 10^{-10} \text{ cm}^2 \text{ s}^{-1}$ in the intermediate discharged state, much higher than that for bare LCO $(\approx 4.05 \times 10^{-11} \text{ cm}^2 \text{ s}^{-1})$, which can be attributed to the reconstructed spinel-like surface with 3D Li+ diffusion channels in DG-LCO (see Figure 1). As shown in Figure S10 (Supporting Information), both LCO and DG-LCO exhibited the decreased impedances with the cycle number, hinting the evolved surface structure. The similar phenomena have been reported^[29] and should be related with the surface structure reconstruction and the activation of bulk structure. Overall, DG-LCO shows much smaller impedance at all selected cycles than LCO, indicating the better surface structure. The rate capability was compared between bare LCO and DG-LCO (Figure 2b). The bare LCO exhibited discharge capacities of 217.9, 190.6, 146, 122.7, 95.5, 61.5, and 35.3 mA h g⁻¹ at 0.1, 0.2, 0.5, 1, 2, 5, and 10 C, respectively, while the DG-LCO showed the higher discharge capacities of 216.3, 213.1, 200, 191.3, 166, 144.1, and 108.1 mA h g⁻¹, respectively. Above results evidently prove the ultrafast Li+ extraction/insertion kinetics, which can be ascribed to the 3D Li⁺ diffusion channels in the unique dual gradient co-lattice spinel surface.

Long-term cycling stability at a high cutoff voltage up to 4.5 V or even 4.6 V is a challenge for current commercial LCO cathodes. The cycling stability in the voltage range of 3.0-4.5 V was evaluated at 0.2 C. DG-LCO exhibited an initial capacity of 199.0 mA h g⁻¹ and delivered 188.6 mA h g⁻¹ capacity with 94.8% retention rate after 200 cycles, while the bare LCO can only delivered 105.9 mA h g⁻¹ capacity with 53.7% retention rate (Figure S11, Supporting Information). To evaluate the long-term cycling stability of cathodes, LCO and DG-LCO were further tested at 0.5 C in 3-4.5 V. As shown in Figure S12 (Supporting Information), DG-LCO cathode delivered an initial capacity of 175.1 mA h g^{-1} and a capacity of 162.6 mA h g^{-1} after 900 cycles at 0.5 C, corresponding to an superior high capacity retention rate of 92.9%.[30] For comparison, the bare LCO can only deliver 73.4 mA h g⁻¹ capacity after 300 cycles, corresponding to a capacity retention rate of 42.7%. The corresponding chargedischarge profiles at different cycles are displayed in Figure S13 (Supporting Information).

When the upper cut-off voltage was further increased to 4.6 V, as shown in Figure 2c,d, DG-LCO delivered a capacity of 170.8 mA h g⁻¹ with a retention rate of 86.9% and an average voltage decay of 0.08 V after 200 cycles at 0.5 C at room temperature. In comparison, the capacity of bare LCO decreased to 102.0 mA h g⁻¹ with only 51.2% retention rate and a much severer decay of 0.28 V in the average voltage. Furthermore, DG-LCO presented a higher coulombic efficiency than bare LCO, suggesting less interfacial electrolyte decomposition reaction and a higher energy conversion efficiency. The corresponding charge-discharge profiles at different cycles for bare LCO and DG-LCO are presented in Figure S14 (Supporting Information). In order to explore the potential application of the cathodes in extreme conditions, long-term cycling measurements were carried out at 0 and 45 °C (Figure 2e). When cycled at 0 °C, DG-LCO showed a capacity retention rate of 83.4% after 100 cycles at 0.2 C, in sharp contrast to bare LCO (49.9%). When cycled at 45 °C, DG-LCO achieved a capacity retention rate of 87.5% after 100 cycles and 79.4% after 200 cycles at 2 C, whereas in LCO these values were only 49% and 35.4%, respectively.

For the scalable production, pouch full cells were assembled with DG-LCO cathodes and mesocarbon microbeads (MCMB) anodes in the negative/positive (N/P) ratio of 1.14:1, and cycled at room temperature in the voltage range of 3.0–4.55 V (equivalent to 3.05–4.6 V vs Li/Li $^{\rm +}$) at 1 C. As shown in Figure 2f, DG-LCO pouch full cells delivered a capacity of 1800 mA h with a retention rate of 88.6% after 100 cycles. All these results demonstrate that, DG-LCO offers both high rate capability and cycling stability for all climates.

2.3. Suppressed Surface Side Reactions

To validate the suppressed surface side reactions by the dual gradient design, in situ differential electrochemical mass spectroscopy (DEMS) was conducted to monitor the release of gaseous O2 and CO2 during the first charge-discharge process. As displayed in Figure 3a, there is an obvious CO2 signal peak from bare LCO at high voltages, coming from the side reaction between the carbonate-based electrolyte and the Co⁴⁺ and O⁻ species at the surface of LCO. In contrast, no detectable CO₂ gas can be observed for DG-LCO (Figure 3b), indicating that the surface side reaction was effectively suppressed. To further investigate the surface chemical property of bare LCO and DG-LCO, surface-sensitive XPS and soft X-ray absorption spectra (sXAS) in TEY mode were adopted.[31] The redox behavior of Co and O were investigated by the XPS spectra of Co 2p and O 1s, as well as the Co L-edge and O K-edge sXAS. As shown in Figure S15 (Supporting Information), there is an obvious peak shoulder at 782 eV that can be assigned to Co⁴⁺ when charging LCO to 4.6 V. Differently, no Co4+ signal is observed for DG-LCO. Furthermore, Co L-edge sXAS spectra were also collected to validate this point. As shown in Figure S16 (Supporting Information), different from LCO, there is no obvious peak shift in Co L-edge sXAS spectra when charging from 4.5 to 4.6 V for DG-LCO, indicating less Co4+ species at the surface. In O K-edge sXAS, the absorption peak at ≈530.5 and 532 eV in the bare LCO can be related with the electron transition from O 1s to the hole state in O 2p-Co 3d hybridized orbitals (Figure S16c,d, Supporting Information). The broad higher energy peaks above 533.5 eV can be assigned to the transition to the hybridized states of O 2p and Co 4sp orbitals. When charged to 4.6 V, the absorption peaks at ≈529 e V (marked by the magenta arrows) are due to the rehybridizations between O and Co ions with greater effective nuclear charge in the local Co-O bond. [32] Moreover, the shoulder absorption peak in the higher energy region of ≈531.2 eV can be assigned to the higher oxidation state O^{-.[33]} In comparison, the decreased peak intensity at ≈531.2 eV for DG-LCO hints the reduced O⁻ species at the surface. Figure 3c shows the F 1s XPS profiles of bare LCO. The peak at 688 eV can be assigned to the C-F bond of polyvinylidene fluoride (PVDF) binder. In addition, there is a high concentration of LiF (685.5 eV) formed at 4.5 V, which can be related to the decomposition of LiPF₆ in electrolyte.^[34] The LiF peaks also can be observed at 4.3 and 4.4 V (Figure S17, Supporting Information), and there is a continuous increase in the peak intensity from 4.3 to 4.5 V, indicates a continuous electrolyte decomposition reaction. However, the peak intensity of LiF suffered from a sharp decrease when further charged to

16146840, 2022, 20, Downloaded from https://advanced.onlinelibrary.wiley.com/doi/10.1002/aenm.202200813 by University Town Of Shenzhen, Wiley Online Library on [23/11/2025]. See the Terms

and Conditions (https://onlinelibrary.wiley.com/terms

and-conditions) on Wiley Online Library for rules of use; OA articles are governed by the applicable Creative Commons I

www.advancedsciencenews.com

www.advenergymat.de

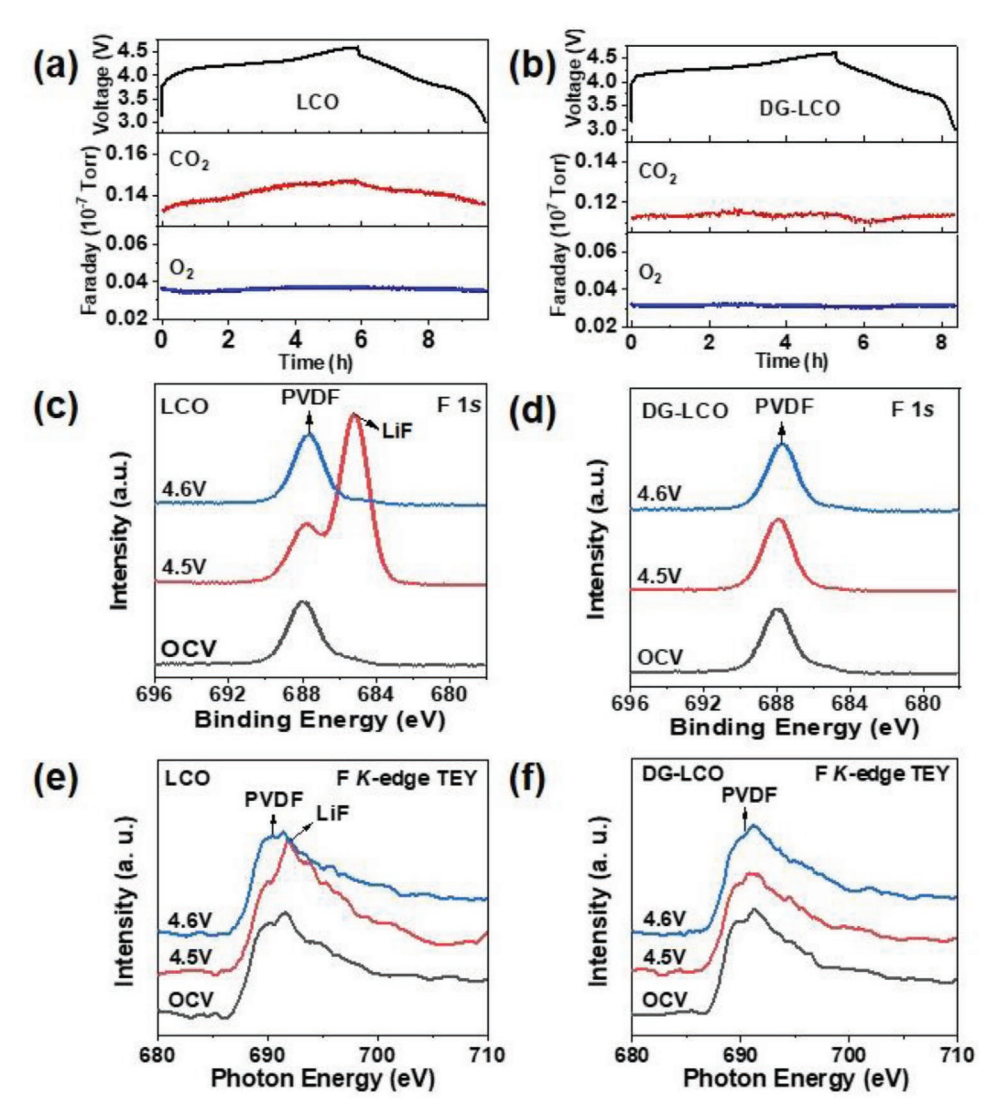


Figure 3. Dual gradient spinel-like surface prevented the interfacial side reaction. In situ DEMS of a) bare LCO and b) DG-LCO during the first charge—discharge process. The F 1s XPS spectra of c) bare LCO and d) DG-LCO at different states of charge. F K-edge sXAS spectra of e) bare LCO and f) DG-LCO under TEY mode at different states of charge.

4.6 V, indicating CEI damage at higher voltage since LiF was considered as one of the main components of CEI. It has been reported that the LiF could decompose when the particle size decreases to nanosize.[35] The similar phenomena of the LiF decomposition at high charge voltage also have been found in previous reports, e. g. Liu's work, [36] Lebens-Higgins' work, [37] Yoon's work,[38] and Cherkashinin's work.[39] The unstable CEI structure (the repeated growth and damage of CEI) would cause a lower Coulombic efficiency (CE) for LCO (see Figure 2c). Moreover, the unsatisfactory interfacial side reaction would even cause irreversible phase transformation of the LCO surface structure and result in a severe capacity degradation upon repeated cycling. In Figure 3e, the F K-edge spectrum of the pristine sample is contributed by the PVDF binder (≈690 eV). When charged to 4.5 V, an obvious shoulder peak appears at ≈692 eV, which can also be ascribed to the LiF species. In comparison, there is no detectable LiF signal in both XPS and sXAS results of DG-LCO (Figure 3d,f). Overall, it is hard to identify the substituted F in DG-LCO due the little amount compared with PVDF, as the F sXAS spectra for OCV samples of LCO and DG-LCO are nearly the same. We deduce that, the decreased amount of lattice ${\rm Co^{4+}}$ and ${\rm O^-}$ species on the particle surface of DG-LCO greatly hindered the decomposition reaction of both carbonate solvent and LiPF $_6$ salt in electrolyte, enhancing the structural stability.

2.4. Enhanced Bulk Structural Stability

As the electrochemical performance is closely related to the structural evolution process upon cycling, ex situ XRD patterns of DG-LCO electrodes at different states of charge during the first cycle were collected to track the structure evolution. Briefly, both bare LCO and DG-LCO experienced similar successive phase transformations through $H1 \rightarrow H2 \rightarrow M1 \rightarrow H3$ as they were discharged from OCV to 3.9, 4.2, 4.4, and 4.5 V,^[7,40]

16146840, 2022, 20, Downloaded from https://advancec

.com/doi/10.1002/aenm.202200813 by University Town Of Shenzhen, Wiley Online Library on [23/11/2025]. See the Terms

and-conditions) on Wiley Online Library for rules of use; OA articles are governed by the applicable Creative Commons

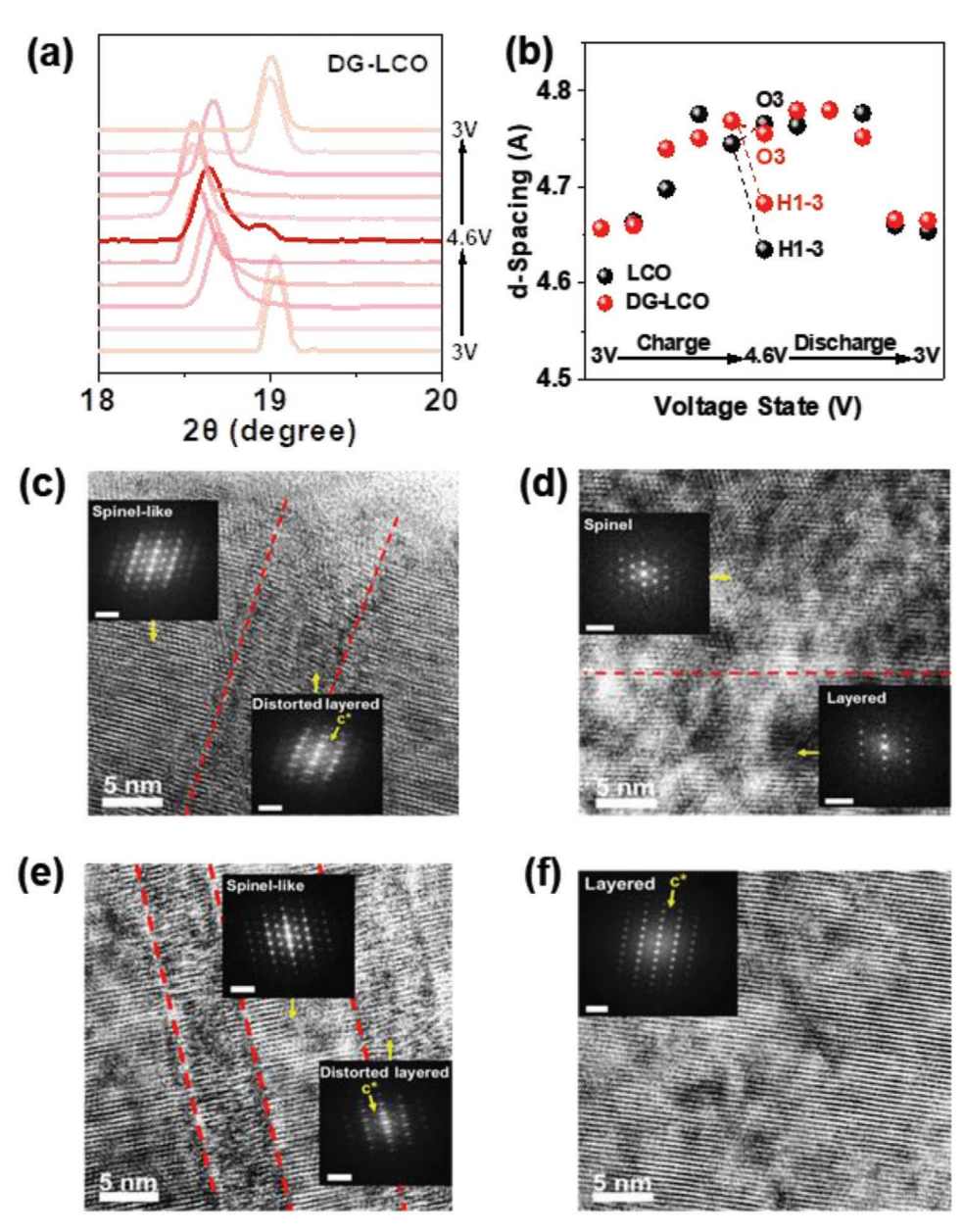


Figure 4. Dual gradient spinel-like surface improved bulk structure stability. The ex situ XRD patterns of a) DG-LCO at different voltage states during the first cycle, and b) corresponding *d*-spacing evolution compared with bare LCO. The voltage points 3.9, 4.2, 4.4, 4.5, and 4.6 V were selected during charge process, and the voltage points 4.4, 4.3, 4.1, 3.8, and 3 V were selected during the discharge process. Cross-sectional HRTEM images of c) bare LCO and d) DG-LCO when first charged to 4.6 V (the insets are the corresponding FFT images, scale bar: 1/5 nm). Cross-sectional HRTEM images of e) bare LCO and f) DG-LCO after 200 cycles (the insets are the corresponding FFT images, scale bar: 1/5 nm).

and obvious phase separation can be observed at 4.6 V, corresponding to the phase transition from H3 to H1-3 (**Figure 4**a and Figures S18 and S19, Supporting Information). To quantitatively compare the phase evolution processes of these two materials, the *d*-spacing of (003) peak was plotted as a function of the charge/discharge state in Figure 4b. At 4.6 V, bare LCO exhibited a severe lattice mismatch between H3 phase and H1-3 phase with $\Delta d = 0.131$ Å, while DG-LCO showed a smaller lattice mismatch with $\Delta d = 0.073$ Å, indicating a suppressed phase transition in DG-LCO.

The lattice mismatch between varied phases tends to induce lattice distortion and severely stress the structure. [42] HRTEM

was used to characterize the structural change of bare LCO and DG-LCO cathodes when charged to 4.6 V. The surface region of bare LCO had transformed to spinel phase (indicated by the FFT map) with obvious lattice distortion in the neighboring layered region. The observed curved fringes indicate severe disordering along the layer-stacking direction and buildups of increasing lattice stress (Figure 4c).^[11] In comparison, the spinel surface of DG-LCO still persisted without inducing severe lattice distortion to the bulk (Figure 4d). To check the corresponding changes of the local structures upon cycling, the HRTEM images for the near-surface regions of LCO and DG-LCO at 10th, 50th, 100th, and 200th cycle were acquired.

www.advancedsciencenews.com

www.advenergymat.de

16146480, 2022, 20, Dwnholaded from https://dwnneed.onlinelibrary.wiely.com/d/010.002/aen.20.2020813 by University Town Of Sheraben, Wiley Online Library on [2311025], See he Terms and Conditions (https://onlinelibrary.wiely.com/terms-and-conditions) on Wiley Online Library for rules of use; OA articles are governed by the applicable Cerative Commons

As displayed in Figure S20 (Supporting Information), after 10 cycles, LCO has a much thicker spinel region at the surface (>20 nm) than DG-LCO (≈10 nm). After 50 cycles, the spinel region for DG-LCO changes a little with sharp reflections in the FFT map while that for LCO becomes disordered with distorted lattice fringes indicated by the dispersed reflection in corresponding FFT map. After 100 cycles, the structural disorder for LCO becomes more serious while DG-LCO still preserves the good crystallinity. The bare LCO and DG-LCO materials after 200 cycles were cut through by FIB and the cross-section morphologies are displayed in Figure S21 (Supporting Information). We can find lots of microcracks through the whole particle of bare LCO, while there were no obvious cracks in DG-LCO. The corresponding HRTEM image clearly shows numerous disordered regions with curved fringes and spinel-like regions in bare LCO after long cycling (Figure 4e). The lattice distortion and spinel phase accumulate especially near the particle surface (Figure S22, Supporting Information). In sharp contrast, DG-LCO can still retain the original layered structure in the bulk (Figure 4f) with a spinel-like surface (Figure S23, Supporting Information). The weaker spots in FFT map can be ascribed to the partial phase transformation from spinel to rock-salt phase, a thermodynamically more stable phase. As reported previously, the rock-salt phase is structural and electrochemically stable at highly delithiated state, thus the formed rock-salt phase can still protect the bulk structure upon cycling.^[43] However, the TM ions in the Li layer would block the Li⁺ diffusion in the rock-salt phase, causing relative low Li⁺ diffusion dynamics and increased polarization, [44] consistent with the charge/discharge profiles of DG-LCO with the cycle number in Figure S14 (Supporting Information). The XPS measurements for DG-LCO were carried out to further investigate the surface structure before cycling and after 200 cycles. As shown in Figure S24 (Supporting Information), the signals for Al show negligible change although the intensities are weak due to the low concentrations, hinting the stable dual gradient surface structure. F 1s XPS spectra for DG-LCO and LCO were also collected in Figure S25 (Supporting Information). LiF signal for DG-LCO is much weaker than that for LCO. It further confirms the protective role of dual gradient strategy, considering that the formation of LiF comes from the surficial side reactions.

3. Conclusion

In summary, we successfully designed and constructed a cation and anion dual gradient spinel-like surface with a thickness around 60 nm in LCO by a wet-coating process followed by medium-temperature calcination. Comprehensive structural characterizations and electrochemical measurements demonstrate that, the dual gradient design greatly reduced Co redox and O redox at the surface and minimized the Co⁴⁺ and O-species when charging to high potentials, thus decreased the related side reactions, making an ultrastable surface structure at 4.6 V high cutoff voltage. In addition, the surface has a spinel structure with the 3D Li⁺ diffusion channels, which enables the fast Li⁺ extraction/insertion kinetics during charge/discharge to achieve ≈ 191 mA h g⁻¹ at 1 C at 4.6 V. All these advantages

make DG-LCO an ultrastable cathode at high potentials, delivering a high capacity retention of 92.9% under a cutoff voltage of 4.5 V after 900 cycles, and also great cycling stability under 4.6 V in the temperature range from 0 to 45 °C. The improved performance is validated in the pouch full cells. Our work unfolds new opportunities to design new cathodes with long lifespan and fast charge capability for high-energy-density lithium-ion batteries.

4. Experimental Section

Material Synthesis: Bare LCO powders were purchased from Xiamen Tungsten New Energy Material Corporation. DG-LCO was prepared by a wet-coating process with 10 mmol LCO, 0.3 mmol $Al(NO_3)_3 \cdot 9H_2O$ (99%, Aladdin) and 1.8 mmol NH_4F (99%, Aladdin) solution with a molar concentration of 0.01 m followed by medium-temperature calcination.

Materials Characterizations: The crystal structure of samples was analyzed by XRD using a Bruker D8 Advance diffractometer (Cu Klpharadiation, $\lambda = 0.154$ nm). Rietveld refinements of XRD patterns were performed using GSAS software packages.[45] The ICP-OES (HORIBA JY2000-2) was conducted for elemental analysis. Morphology and elemental distribution investigation of the samples were conducted using a scanning electron microscope (SEM, Zeiss SUPRA-55) with a X-Max EDS detector. The HRTEM was performed on a JEM-100F microscope. TEM samples were prepared using the FIB. The chemical states of the selected elements were investigated by X-ray photoelectron spectrometry (XPS) on a Thermo Scientific Escalab 250Xi spectrometer. The sXAS measurements were conducted under the total electron yield (TEY) mode in an ultrahigh vacuum chamber at beamline 02B02 of the SiP-ME2 platform, Shanghai Synchrotron Radiation Facility (SSRF). The photon flux was about 1011 photons s⁻¹ and the energy resolving power $E/\Delta E$ was up to 13 000@250 eV.

Electrochemical Testing: The positive electrodes were fabricated with 80 wt% active material, 10 wt% carbon black as the conductive additive, and 10 wt% PVDF (99%, Aladdin) as the binder. Then the powder was dispersed in N-methyl-1, 2-pyrrolidone (NMP, 99%, Aladdin) with continuously stirred for 12 h to obtain a homogeneous slurry. The slurry was then cast onto aluminum foil with a blade and dried at 120 °C in a vacuum oven for 12 h. The mass loading of active material was ≈3 mg cm⁻². 2032-type coin cells were assembled in an argon-filled glovebox with LiCoO2 materials as the cathode materials, lithium foil as the anode, Celgard film as the separator, and 1 M LiPF₆ in ethylene carbonate/dimethyl carbonate (EC/DMC, 1:1 in volume) as the electrolyte. The pouch cells were fabricated with a capacity ratio of negative electrode capacity/positive electrode capacity (N/P ratio) = 1.14:1 with dimensions of 5.6 cm \times 3.3 cm in the pouch-cell production line. The negative electrode was prepared with 92 wt% MCMB, 3 wt% SP (MTI Corporation KJ GROUP) and 5 wt% CMC binder. The positive electrode was fabricated with 92% LCO, 4% CNT, 2% acetylene black, and 2% PVDF binder. The mass loading of active material was ≈22 mg cm⁻². The galvanostatic charge-discharge tests were carried out using a NEWARE battery test system. The CV and electrochemical impedance spectroscopy (EIS) were tested on a Solartron Analytical 1470E electrochemical workstation. The CV curves were obtained at a scan rate of 0.1 mV s⁻¹ in the voltage range of 3.0-4.6 V (vs Li/Li⁺) and the frequency range of EIS was 100 kHz to 0.1 Hz. The GITT was carried out on the Macrro Electrochemical Workstation. In situ DEMS was used to track O2 and CO2 gas evolution during the first cycle.

Supporting Information

Supporting Information is available from the Wiley Online Library or from the author.

ADVANCED ENERGY MATERIALS

16146840, 2022, 20, Downloaded from https://advanced.onlinelibrary.wiley.com/doi/10.1002/aenm.202200813 by University Town Of Shenzhen, Wiley Online Library on [23/11/2025]. See the Terms

and Conditions (https://onlinelibrary.wiley.com/terms-and-conditions) on Wiley Online Library for rules of use; OA articles are governed by the applicable Creative Commons

Acknowledgements

W.H. and Q.Z. contributed equally to this work. This work was financially supported by the National Natural Science Foundation of China (52172175), the Shenzhen Science and Technology Research Grant (JCYJ20200109140416788, JCYJ20210324130812033), the Chemistry and Chemical Engineering Guangdong Laboratory (1922018), the National Key R&D Program of China (2020YFB0704500), and the Major Science and Technology Infrastructure Project of Material Genome Big-science Facilities Platform supported by Municipal Development and Reform Commission of Shenzhen.

Conflict of Interest

The authors declare no conflict of interest.

Data Availability Statement

The data that support the findings of this study are available from the corresponding author upon reasonable request.

Keywords

dual gradient, high voltage, LiCoO₂ cathodes, lithium-ion batteries, stable surface structure

Received: March 8, 2022 Published online: April 10, 2022

- a) M. S. Whittingham, Chem. Rev. 2004, 104, 4271; b) V. Etacheri,
 R. Marom, G. S. Elazari, D. Aurbach, Energy Environ. Sci. 2011, 4, 3243; c) Y. Lyu, X. Wu, K. Wang, Z. Feng, T. Cheng, Y. Liu, M. Wang,
 R. Chen, L. Xu, J. Zhou, Y. Lu, B. Guo, Adv. Energy Mater. 2020, 11, 2000982.
- [2] a) X. Wang, X. Y. Wang, Y. Y. Lu, Ind. Eng. Chem. Res. 2019, 58, 10119;
 b) S. K. Jung, H. Gwon, J. Hong, K. Y. Park, D. H. Seo, H. Kim, J. Hyun, W. Yang, K. Kang, Adv. Energy Mater. 2014, 4, 7.
- [3] a) M. D. Radin, S. Hy, M. Sina, C. C. Fang, H. D. Liu, J. Vinckeviciute, M. H. Zhang, M. S. Whittingham, Y. S. Meng, A. Van der Ven, Adv. Energy Mater. 2017, 7, 1602888; b) R. Gu, Z. T. Ma, T. Cheng, Y. C. Lyu, A. M. Nie, B. K. Guo, ACS Appl. Mater. Interfaces 2018, 10, 31271.
- [4] S. Kalluri, M. Yoon, M. Jo, S. Park, S. Myeong, J. Kim, S. X. Dou, Z. P. Guo, J. Cho, Adv. Energy Mater. 2017, 7, 21.
- [5] K. Mizushima, P. C. Jones, P. J. Wiseman, J. B. Goodenough, *Mater. Res. Bull.* 1980, 15, 783.
- [6] Z. H. Chen, J. R. Dahn, Electrochim. Acta 2004, 49, 1079.
- [7] G. G. Amatucci, J. M. Tarascon, L. C. Klein, J. Electrochem. Soc. 1996, 143, 1114
- [8] Q. Yang, J. Huang, Y. J. Li, Y. Wang, J. L. Qiu, J. N. Zhang, H. G. Yu, X. Q. Yu, H. Li, L. Q. Chen, J. Power Sources 2018, 388, 65.
- [9] Q. Liu, X. Su, D. Lei, Y. Qin, J. Wen, F. Guo, Y. A. Wu, Y. Rong, R. Kou, X. Xiao, F. Aguesse, J. Bareño, Y. Ren, W. Lu, Y. Li, *Nat. Energy* 2018, 3, 936.
- [10] a) L. Wang, J. Ma, C. Wang, X. Yu, R. Liu, F. Jiang, X. Sun, A. Du, X. Zhou, G. Cui, Adv. Sci. 2019, 6, 1900355; b) J.-N. Zhang, Q. Li, C. Ouyang, X. Yu, M. Ge, X. Huang, E. Hu, C. Ma, S. Li, R. Xiao, W. Yang, Y. Chu, Y. Liu, H. Yu, X.-Q. Yang, X. Huang, L. Chen, H. Li, Nat. Energy 2019, 4, 594.
- [11] J. Li, C. Lin, M. Weng, Y. Qiu, P. Chen, K. Yang, W. Huang, Y. Hong, J. Li, M. Zhang, C. Dong, W. Zhao, Z. Xu, X. Wang, K. Xu, J. Sun, F. Pan, Nat. Nanotechnol. 2021, 16, 599.

- [12] Z. Zhu, H. Wang, Y. Li, R. Gao, X. Xiao, Q. Yu, C. Wang, I. Waluyo, J. Ding, A. Hunt, J. Li, Adv. Mater. 2020, 32, 50.
- [13] a) J. Kikkawa, S. Terada, A. Gunji, T. Nagai, K. Kurashima, K. Kimoto, J. Phys. Chem. C 2015, 119, 15823; b) M. Yoon, Y. Dong, Y. Yoo, S. Myeong, J. Hwang, J. Kim, S. H. Choi, J. Sung, S. J. Kang, J. Li, J. Cho, Adv. Funct. Mater. 2020, 30, 11; c) Y. J. Kim, J. P. Cho, T. J. Kim, B. Park, J. Electrochem. Soc. 2003, 150, A1723; d) S. H. Min, M. R. Jo, S. Y. Choi, Y. I. Kim, Y. M. Kang, Adv. Energy Mater. 2016, 6. 13.
- [14] a) H. Xia, L. Lu, Y. S. Meng, G. Ceder, J. Electrochem. Soc. 2007, 154, A337; b) Y. H. Xu, E. Y. Hu, K. Zhan, X. L. Wang, V. Borzenets, Z. H. Sun, P. Pianetta, X. Q. Yu, Y. J. Liu, X. Q. Yang, H. Li, ACS Energy Lett. 2017, 2, 1240; c) P. F. Yan, J. M. Zheng, T. W. Chen, L. L. Luo, Y. Y. Jiang, K. Wang, M. L. Sui, J. G. Zhang, S. L. Zhang, C. M. Wang, Nat. Commun. 2018, 9, 8.
- [15] Y. Liu, X. J. Lin, Y. G. Sun, Y. S. Xu, B. B. Chang, C. T. Liu, A. M. Cao, L. J. Wan, Small 2019, 15, 17.
- [16] J. Qian, L. Liu, J. Yang, S. Li, X. Wang, H. L. Zhuang, Y. Lu, Nat. Commun. 2018, 9, 4918.
- [17] a) Y. Wang, Q. Zhang, Z. C. Xue, L. Yang, J. Wang, F. Meng, Q. Li, H. Pan, J. N. Zhang, Z. Jiang, W. Yang, X. Yu, L. Gu, H. Li, Adv. Energy Mater. 2020, 10, 2001413; b) K. H. Nie, X. L. Wang, J. L. Qiu, Y. Wang, Q. Yang, J. J. Xu, X. Q. Yu, H. Li, X. J. Huang, L. Q. Chen, ACS Energy Lett. 2020, 5, 826.
- [18] a) Y. S. Jung, A. S. Cavanagh, A. C. Dillon, M. D. Groner,
 S. M. George, S. H. Lee, J. Electrochem. Soc. 2010, 157, A75;
 b) T. Cheng, Z. Ma, R. Qian, Y. Wang, Q. Cheng, Y. Lyu, A. Nie,
 B. Guo, Adv. Funct. Mater. 2020, 31, 2001974.
- [19] a) M. Murakami, H. Yamashige, H. Arai, Y. Uchimoto, Z. Ogumi, Electrochim. Acta 2012, 78, 9614; b) Y. Zhou, Y. H. Lee, H. X. Sun, J. M. Wallas, S. M. George, M. Xie, ACS Appl. Mater. Interfaces 2017, 9, 9614.
- [20] R. Gu, T. Cheng, Z. T. Ma, R. C. Qian, Y. C. Lyu, A. M. Nie, B. K. Guo, J. Alloys Compd. 2019, 803, 348.
- [21] a) M. Wang, X. Feng, H. Xiang, Y. Feng, C. Qin, P. Yan, Y. Yu, Small Methods 2019, 3, 1900355; b) A. Aboulaich, K. Ouzaouit, H. Faqir, A. Kaddami, I. Benzakour, I. Akalay, Mater. Res. Bull. 2016, 73, 362.
- [22] Z. Zhu, D. Yu, Z. Shi, R. Gao, X. Xiao, I. Waluyo, M. Ge, Y. Dong, W. Xue, G. Xu, W. K. Lee, A. Hunt, J. Li, Energy Environ. Sci. 2020, 13, 1865.
- [23] a) Y. I. Jang, B. Y. Huang, H. F. Wang, D. R. Sadoway, G. Ceder, Y. M. Chiang, H. Liu, H. Tamura, J. Eelectrochem. Soc. 1999, 146, 862; b) H. T. Xu, H. J. Zhang, L. Liu, Y. Y. Feng, Y. Wang, ACS Appl. Mater. Interfaces 2015, 7, 20979; c) Z. Z. Cui, Z. Y. Wang, Y. W. Zhai, R. Gao, Z. B. Hu, X. F. Liu, J. Nanosci. Nanotechnol. 2020, 20, 2473.
- [24] C. M. Subramaniyam, H. Celio, K. Shiva, H. C. Gao, J. B. Goodenough, H. K. Liu, S. X. Dou, Sustainable Energy Fuels 2017, 1, 1292.
- [25] a) H. G. Jung, N. V. Gopal, J. Prakash, D. W. Kim, Y. K. Sun, Electrochim. Acta 2012, 68, 153; b) P. Yue, Z. X. Wang, H. J. Guo, X. H. Xiong, X. H. Li, Electrochim. Acta 2013, 92, 1; c) D. M. Liu, X. J. Fan, Z. H. Li, T. Liu, M. H. Sun, C. Qian, M. Ling, Y. J. Liu, C. D. Liang, Nano Energy 2019, 58, 786; d) P. Vanaphuti, J. J. Chen, J. Y. Cao, K. Bigham, B. Chen, L. F. Yang, H. L. Chen, Y. Wang, ACS Appl. Mater. Interfaces 2019, 11, 37842; e) Z. Si, B. Z. Shi, J. Huang, Y. Yu, Y. Han, J. L. Zhang, W. Li, J. Mater. Chem. A 2021, 9, 9354.
- [26] M. S. Idris, A. R. West, J. Electrochem. Soc. 2012, 159, A396.
- [27] a) Y. M. Huang, Y. H. Dong, S. Li, J. Lee, C. Wang, Z. Zhu, W. J. Xue, Y. Li, J. Li, Adv. Energy Mater. 2021, 11, 2000997; b) L. Zhang, W. He, D.-L. Peng, Q. S. Xie, R.-J. Xie, ChemElectroChem 2019, 6, 1542; c) X. L. Li, D. Li, D. W. Song, X. X. Shi, X. Tang, H. Z. Zhang, L. Q. Zhang, ACS Appl. Mater. Interfaces 2018, 10, 8827; d) F. Wu, W. K. Li, L. Chen, J. Wang, W. Bao, Y. Lu, J. Tan, S. Chen, R. J. Chen, Y. F. Su, J. Power Sources 2018, 402, 499; e) Y. Pei, C.-Y. Xu, Y.-C. Xiao, Q. Chen, B. Huang, B. Li, S. Li, L. Zhen, G. Cao, Adv. Funct. Mater.



ADVANCED ENERGY

www.advancedsciencenews.com www.advenergymat.de

2017, *27*, 1604349; f) M. Xu, L. Fei, W. Lu, Z. Chen, T. Li, Y. Liu, G. Gao, Y. Lai, Z. Zhang, P. Wang, H. Huang, *Nano Energy* **2017**, *35*, 271; g) R. Gu, Z. Ma, T. Cheng, Y. Lyu, A. Nie, B. Guo, *ACS Appl. Mater. Interfaces* **2018**, *10*, 31271; h) J. H. Shim, K. S. Lee, A. Missyul, J. Lee, B. Linn, E. C. Lee, S. Lee, *Chem. Mater.* **2015**, *27*, 3273.

- [28] A. Van der Ven, M. K. Aydinol, G. Ceder, G. Kresse, J. Hafner, Phys. Rev. B 1998, 58, 2975.
- [29] a) L. S. Wang, Y. D. Huang, D. Z. Jia, Solid State Ionics 2006, 177, 1477; b) X. Ji, X. Y. Dai, F. Z. Wu, Y. Mai, H. J. Chen, Y. J. Gu, Ceram. Int. 2021, 47, 32043.
- [30] a) T. Tian, T. W. Zhang, Y. C. Yin, Y. H. Tan, Y. H. Song, L. L. Lu, H. B. Yao, Nano Lett. 2019, 20, 677; b) Z. Li, A. Li, H. Zhang, F. Ning, W. Li, A. Zangiabadi, Q. Cheng, J. J. Borovilas, Y. Chen, H. Zhang, X. Xiao, C. Ouyang, X. Huang, W. K. Lee, M. Ge, Y. S. Chu, X. Chuan, Y. Yang, Energy Storage Mater. 2020, 29, 71.
- [31] Z. Q. Zhuo, F. Pan, W. L. Yang, Chin. J. Struct. Chem. 2019, 38, 2009.
- [32] W. S. Yoon, K. B. Kim, M. G. Kim, M. K. Lee, H. J. Shin, J. M. Lee, J. Phys. Chem. B 2002, 106, 2526.
- [33] X. Cao, H. F. Li, Y. Qiao, M. Jia, X. Li, J. Cabana, H. S. Zhou, Adv. Mater. 2020, 2004280.
- [34] a) Y. J. Bi, T. Wang, M. Liu, R. Du, W. C. Yang, Z. X. Liu,
 Z. Peng, Y. Liu, D. Y. Wang, X. L. Sun, RCS Adv. 2006, 6, 19233;
 b) Z. W. Lebens-Higgins, S. Sallis, N. V. Faenza, F. Badway,
 N. Pereira, D. M. Halat, M. Wahila, C. Schlueter, T. L. Lee, W. L. Yang,
 C. P. Grey, G. G. Amatucci, L. F. J. Piper, Chem. Mater. 2018, 30, 958.
- [35] H. Li, G. Richter, J. Maier, Adv. Mater. 2003, 15, 736.
- [36] S. Y. Liu, L. D. Y. Wang, C. C. Zhang, B. B. Chu, C. P. Wang, T. Huang, A. S. Yu, J. Power Sources 2019, 438, 226979.
- [37] Z. W. Lebens-Higgins, S. Sallis, N. V. Faenza, F. Badway, N. Pereira, D. M. Halat, M. Wahila, C. Schlueter, T. L. Lee, W. L. Yang, C. P. Grey, G. G. Amatucci, L. F. J. Piper, Chem. Mater. 2018, 30, 958.

- [38] a) T. Yoon, D. Kim, K. H. Park, H. Park, S. Jurng, J. Jang, J. H. Ryu, J. J. Kim, S. M. Oh, J. Electrochem. Soc. 2014, 161, A519; b) T. Yoon, T. Lee, J. Soon, H. Jeong, S. Jurng, J. H. Ryu, S. M. Oh, J. Electrochem. Soc. 2018, 165, A1095; c) T. Yoon, J. Y. Soon, T. J. Lee, J. H. Ryu, S. M. Oh, J. Power Sources 2021, 503, 230051.
- [39] G. Cherkashinin, K. Nikolowski, H. Ehrenberg, S. Jacke, L. Dimesso, W. Jaegermann, Phys. Chem. Chem. Phys. 2012, 14, 12321.
- [40] a) L. L. Wang, B. B. Chen, J. Ma, G. L. Cui, L. Q. Chen, Chem. Soc. Rev. 2018, 47, 6505; b) A. Yano, M. Shikano, A. Ueda, H. Sakaebe, Z. Ogumi, J. Electrochem. Soc. 2017, 164, A6116.
- [41] a) Z. H. Chen, Z. H. Lu, J. R. Dahn, J. Electrochem. Soc. 2002, 149, A1604; b) W. M. Seong, K. Yoon, M. H. Lee, S. K. Jung, K. Kang, Nano Lett. 2019, 19, 29; c) M. Hirooka, T. Sekiya, Y. Omomo, M. Yamada, H. Katayama, T. Okumura, Y. Yamada, K. Ariyoshi, J. Power Sources 2020, 463, 8.
- [42] a) S. M. Bak, Z. Shadike, R. Q. Lin, X. Q. Yu, X. Q. Yang, NPG Asia Mater. 2018, 10, 18; b) J. X. Zheng, T. C. Liu, Z. X. Hu, Y. Wei, X. H. Song, Y. Ren, W. D. Wang, M. M. Rao, Y. Lin, Z. H. Chen, J. Lu, C. M. Wang, K. Amine, F. Pan, J. Am. Chem. Soc. 2016, 138, 13326.
- [43] a) W. Liu, P. Oh, X. E. Liu, S. Myeong, W. Cho, J. Cho, Adv. Energy Mater. 2015, 5, 1500274; b) T. Cheng, Z. T. Ma, R. C. Qian, Y. T. Wang, Q. Cheng, Y. C. Lyu, A. M. Nie, B. K. Guo, Adv. Funct. Mater. 2020, 2001974; c) Z. Si, B. Z. Shi, J. Huang, Y. Yu, Y. Han, J. L. Zhang, W. Li, J. Mater. Chem. A 2021, 9, 9354.
- [44] a) W. Liu, P. Oh, X. E. Liu, S. Myeong, W. Cho, J. Cho, Adv. Energy Mater. 2015, 5, 1500274; b) M. Yoon, Y. H. Dong, Y. Yoo, S. Myeong, J. Hwang, J. Kim, S. H. Choi, J. Sung, S. J. Kang, J. Li, J. Cho, Adv. Funct. Mater. 2020, 30, 1907903.
- [45] a) B. H. Toby, J. Appl. Crystallogr. 2001, 34, 210; b) A. C. Larson, R. B. V. Dreele, General Structure Analysis System (GSAS), LAUR 86-748, Los Alamos National Laboratory, 2000.